J Solid State Electrochem (2011) 15:2265–2275
DOI 10.1007/s10008-010-1236-0

ORIGINAL PAPER

Morphological, electrochemical and photoelectrochemical characterization of nanotubular TiO_2 synthetized electrochemically from different electrolytes

Diego P. Oyarzún · Ricardo Córdova · Omar E. Linarez Pérez · Eduardo Muñoz · Rodrigo Henríquez · Manuel López Teijelo · Humberto Gómez

Received: 11 August 2010 / Revised: 2 November 2010 / Accepted: 4 November 2010 / Published online: 25 November 2010

Abstract The electrochemical synthesis of auto-organized TiO_2 arrays generated by Ti anodization in different non-aqueous electrolytes was analyzed. Propylene carbonate-based electrolytes seem to be good electrolytic media for the controlled growth of titania nanotube structures. Scanning electron microscopy (SEM) analysis indicated that, depending on the media employed in the synthesis of the TiO_2 nanotubes, different aspect ratios (length/diameter) could be obtained. Impedance analysis using the passive pit model gave the electrical properties of the layers during the different stages of nanotubes formation. Mott–Schottky analysis and the impedance results showed that the TiO_2 nanotubes layers were n-type semiconductors with highly defective walls on top of a resistive barrier layer. Photoelectrochemical measurements showed that tetra(4-carboxyphenyl)porphyrin (TCPP) adsorbed onto the TiO_2 nanotube arrays, which could be employed as an efficient photosensitizer for solar-energy conversion by TCPP-sensitized nanotubular TiO_2 electrodes.

Keywords Titania nanotubes · Impedance spectroscopy; · Semiconductors · Dye sensitizers

D. P. Oyarzún (✉) · R. Córdova · E. Muñoz · R. Henríquez · H. Gómez
Instituto de Química, Facultad de Ciencias,
Pontificia Universidad Católica de Valparaíso,
Av. Brasil 2950,
Valparaíso, Chile
e-mail: diequim@gmail.com

O. E. Linarez Pérez · M. López Teijelo
INFIQC – Departamento de Fisicoquímica, Facultad de Ciencias Químicas, Universidad Nacional de Córdoba,
Haya de la Torre y Medina Allende,
5000, Córdoba, Argentina

Introduction

The controlled manufacture of nanometric-scale structures is an area of interest in nanotechnology. In the past several decades, auto-organized nanostructures of different metals and semiconductors have received considerable attention because these materials have a potential for technological use [1]. One of the most studied metallic compounds is aluminum oxide [2–4]. It is well known that highly ordered porous structures can be generated under different anodization conditions. Recently, it has been shown that, by employing optimized electrochemical conditions, auto-organized porous structures can also be obtained on other metallic substrates, including Ti [1, 5–17], Zr [18, 19], Nb [20, 21], W [22, 23], Ta [24, 25] and Hf [26]. Within this group of metals, it has been demonstrated that titanium anodization in electrolytic baths containing fluoride ions is the route to manufacture highly ordered nanotubes with interesting properties [1, 27, 28]. Under these conditions, it is possible to generate ordered structures with different properties, such as pore diameter, length and thickness of walls, by modifying the electrochemical conditions. Consequently, nanotube arrays of titanium oxide offer potential uses in diverse areas, such as the manufacture of gas and biomolecules sensor devices [29, 30], charge storage devices [31], biocompatible materials for dental and osseous implants [32], photocatalysis and photovoltaic systems [27, 33, 34].

The versatility of the properties of TiO_2 nanostructures is mainly due to their high surface/volume relation because their properties strongly depend on their size. The optimization of the properties of TiO_2 nanotubes requires an understanding of the formation mechanisms and the factors that determine the morphology. A direct relationship exists between the formation conditions (applied voltage–time

program, time of anodization, temperature, organic solvents, amount of H_2O, supporting electrolyte, donor fluoride ion species and counterion, pH, viscosity, cathode material, annealing treatment after anodizing, etc.) and the nanotube geometry (diameter, width of the walls, length, space distribution, and pore density) and their properties [1, 9–17, 35–40].

Extensive work has been done to obtain a better understanding of the mechanism involved in nanotube array growth. The evolution of the synthesis of TiO_2 nanotube films had two main stages. In the first stage, nanotube arrays were obtained in aqueous solutions of hydrofluoric acid. However, the film dissolution increased due to the high local proton concentration, and, as a result, the nanotubes had short lengths (<500 nm) [6–9, 18, 36]. To minimize the dissolution process, the hydrofluoric acid was replaced by fluoride salts that have buffer capabilities (i.e., NaF, KF and NH_4F). In this case, it is possible to adjust the pH gradient inside the tubes, and thus, the tube lengths reach up to 5 μm [10–14]. Soluble complex formation, due to the presence of fluoride ions, is another important aspect, and it is postulated that the length of the nanotubes is dependent on the diffusion of fluoride ions into the pores. In the second stage, to control the diffusion process, non-aqueous solvents (i.e., glycerol, ethylene glycol, dimethyl sulphoxyde) lead to longer and smoother nanotubes [1, 10, 12, 13, 17, 27, 35, 38]. The key to achieving high aspect ratio (length/diameter) growth is to adjust the dissolution rate of TiO_2 by localized acidification at the pore bottom, while a protective environment is maintained along the pore walls and at the pore mouth [7, 37, 39].

At present, a critical aspect of science and technology is the efficient use of solar energy [27]. Within the new materials developed for photoelectrolysis applications, TiO_2 is one of the most promising due to its high efficiency, low cost, and chemical and photo-stability. However, the technological use of titanium oxide is limited by its wide band-gap (approximately 3.2 eV), which requires UV irradiation for its photocatalytic activation. Historically, the TiO_2 doping with metals has been used to improve the conductive properties of this material to prevent the electron–hole recombination process without loss of the integrity of the crystalline structure [41, 42]. Recently, studies on the electron transfer and transport processes in solar cells with colored substances (dye-sensitized cells) consisting of nanocrystalline TiO_2 with high efficiencies for solar energy to electrical energy have been reported [27, 44–46].

In the present work, we report the electrochemical synthesis of self-organized nanostructures of porous TiO_2 generated by means of the anodization of Ti in different electrolytic baths, as well as their morphology and electrochemical and photoelectrochemical properties.

Experimental

Titanium anodization was performed in a cell with a two-electrode arrangement. The working electrodes consisted of polycrystalline titanium foils (Aldrich, 99.99% purity) of 250 μm in thickness (1 cm^2 of exposed geometric area) mounted on Teflon holders. A titanium sheet of 4×5 cm^2 was used as the counter electrode. Prior to anodization, the samples were degreased by sonication in a 50:50 acetone/ethanol mixture for 15 min. After the cleaning, the foils were rinsed with deionized water and dried under an argon stream. Anodization experiments were carried out using a DYME high-voltage power supply (150 V/2 A) model with an RS-232 PC interface. The anodic growth of the titanium oxide films was performed by direct anodic polarization of the cleaned titanium surfaces by applying a voltage step up to different voltage values (U_a) in the range of 20–80 V. Measurements were performed at a constant temperature in the range of 5–40 °C with continuous stirring. The electrolytic solutions were prepared from analytical grade reagents and were based on ethylene glycol, dimethyl sulphoxyde and propylene carbonate, x% w/w fluoride ammonium ($0.2\leq x \leq1$) and y% v/v water ($1.5\leq y \leq5$). A subsequent thermal annealing of the oxide layers was carried out at 450 °C in air for 3 h to convert the amorphous oxide to the anatase allotropic form.

For electrochemical and photoelectrochemical studies, a conventional three-electrode cell was employed with a platinum wire as a counter electrode and with a mercury/mercury sulphate electrode (MSE) (Hg/Hg_2SO_4, K_2SO_4 saturated 0.640 V vs. SHE) as a reference electrode. All the potential values are referred to the standard hydrogen electrode (SHE). Electrochemical impedance spectroscopy (EIS) measurements were carried out using a Zahner IM6 potentiostat. Mott–Schottky (MS) plots were obtained at 10 kHz and an AC amplitude of 10 mV using a Zahner IM6e potenciostat. Photoelectrochemical measurements were performed using a Solar Simulator system as an illumination source. All measurements were carried out under solar simulation conditions, with a UV enhanced xenon lamp of 150 W (Newport Oriel Instruments 6254) mounted in a lamp holder (Oriel 67005) connected to a water filter (Oriel 61945) and then connected to the cell with 1 m of optical fiber (Oriel 77578). A power supply of 40–200 W (Oriel 68907) was used to generate the arc in the lamp. The illumination power was quantified inside the cell by means an energy radiant meter (Oriel 70260). The samples were illuminated at a constant light intensity of 4.0 $mW\,cm^{-2}$. The sensitization of the surfaces was performed by overnight dipping (24 h) in a 0.25-mM TCPP ethanolic solution. A pure argon stream was passed through the solution for 30 min before measurements and over the solution when the experiments were under way. In

the impedance (EIS, MS plots) and photoelectrochemical experiments, a 0.1 M KCl aqueous solution was employed.

The surface morphology of the nanostructured layers was characterized by scanning electron microscopy (SEM) using a SEM LEO 1420VP model.

Results and discussion

Anodic growth of TiO_2 nanotubes

Figure 1 shows SEM images obtained for anodic oxide films formed at voltage values of 30 V (Fig. 1a) or 60 V (Fig. 1b). The potential was applied for 3 h at 20 °C to a titanium foil immersed in 0.2% w/w NH_4F + 3% v/v H_2O solution in ethylene glycol. A highly ordered self-assembled nanotube array was obtained for both conditions, and the diameters of the tubes were around 90 nm for U_a= 30 V and 160 nm for U_a=60 V. It has been previously demonstrated for TiO_2, ZrO_2 and Nb_2O_5 nanotube layers that there is a linear dependence between the tube diameter and the voltage applied [1]. In addition, due to the significant IR drop that occurs in non-aqueous electrolytes, it was necessary to apply a higher voltage to generate well-defined nanotubular structures because the morphology and the degree of self-organization are dependent on the voltage applied (see discussion below).

Figure 2 shows a top-view image of a titanium foil anodized for 8 h at a constant voltage of 60 V in a dimethyl sulphoxide solution containing 0.2% w/w NH_4F and 3% v/v H_2O at 20 °C (Fig. 2a) and 40 °C (Fig. 2b). At room temperature, a heterogeneous-cracked surface with cylindrical nanotubes clustered together can be clearly observed. At higher temperatures, the tubes are separated, and they have a greater diameter. Mor et al. [27] postulated that the cracks are the result of surface stress, which originates during the formation of the oxide films. Such cracks are not apparent in the films prepared by the anodization of Ti in aqueous electrolytes, possibly due to the rapid oxide formation. In addition, when the temperature was raised to 40 °C (Fig. 2b), the nanotubes had a smaller diameter in the mouth than in the middle length, generating a drop vessel shape. This observation indicates that etching takes place preferentially in the inner zones of the tubes due to the higher fluoride diffusion promoted by the temperature and the solvent polarity. However, the length and quality of the nanotube layers obtained in dimethyl sulphoxyde were lower than those obtained using ethylene glycol-based solutions for similar electrolysis conditions [12, 13, 17, 27].

Because of its physical properties, propylene carbonate seems to be another good solvent for TiO_2 nanotube growth. Its higher viscosity compared with water might permit the control of the fluoride transport inside the tubes, as in the case of ethylene glycol. Additionally, propylene carbonate is a non-polar protic solvent like dimethyl sulphoxyde, and the ion conductivity may play an important role in the growth of anodic layers. Figure 3 shows morphological top views and lateral views (inset in each figure) of the oxide layers formed in different conditions using propylene carbonate based solutions. Oxide layers formed in the absence of ethylene glycol (Fig. 3a) are homogeneous, compact and almost flat, whereas the titania layers grown in the mixed solutions show self-assembling of TiO_2 nanotube structures (Fig. 3b and c). The absence of nanotubes in pure propylene carbonate could be attributed to the low solubility of the fluoride complex in this solvent, given that the electrolyte contains a minimal quantity of water. In contrast, self-assembled TiO_2 nanotube arrays are obtained for different anodization conditions when ethylene glycol is added to the electrolyte (Fig. 3b and c). Despite the different applied voltage and temperature, by comparing Fig. 3a and b, the generation of tubular nanostructures is directly related to the presence of ethylene glycol. No appreciable change in the thickness of the film was observed due to the modification in the electrolyte composition (~200 μm). As described above, the magnitude of the voltage has an effect on the diameter of the tubes [1]. On the other hand, an increase in the temperature would increase both the growth and dissolution rates, and, therefore, the shape of the nanotubes would be modified. These two effects were not observed.

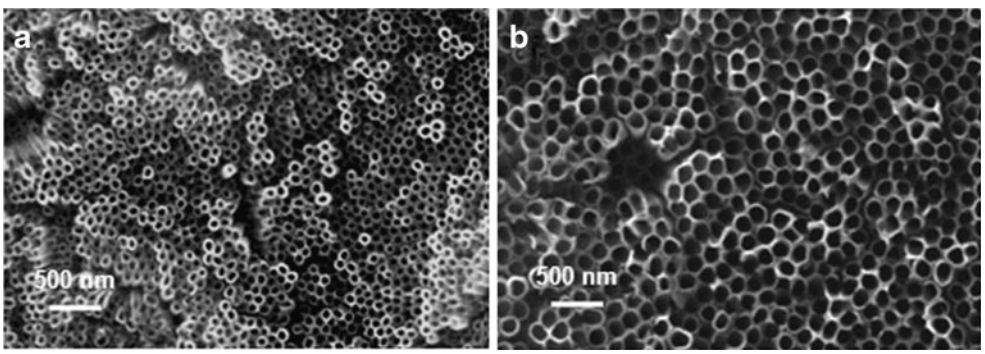

Fig. 1 Top view SEM images for anodized Ti during 3 h at 20 °C in ethylene glycol containing 0.2% w/w NH_4F and 3% v/v H_2O for U_a=30 V **a** and 60 V (**b**)

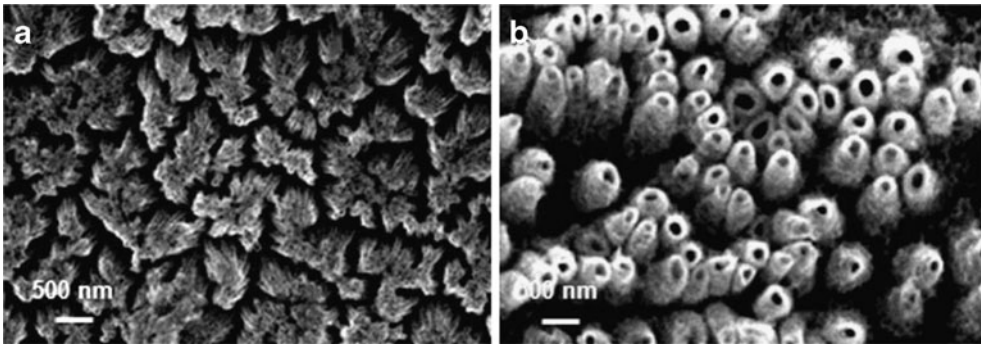

Fig. 2 Top view SEM images for anodized Ti during 8 h with U_a=60 V in dimethyl sulphoxyde containing 0.2% w/w NH_4F and 3% v/v H_2O at 20 °C **a** and 40 °C (**b**)

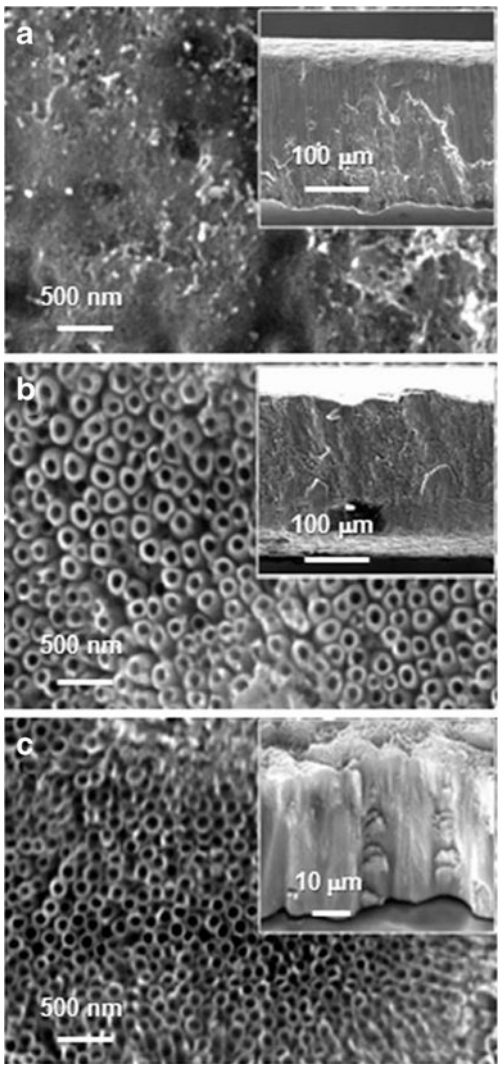

Fig. 3 Top view SEM images for anodic TiO_2 layers obtained under different conditions: **a** propylene carbonate containing 0.2% w/w NH_4F and 3% v/v H_2O, U_a=60 V, t_a=6 h and T=20 °C; **b** 50:50 propylene carbonate/ethylene glycol containing 0.2% w/w NH_4F and 3% v/v H_2O, U_a=80 V, t_a=6 h and T=5 °C; **c** 50:50 propylene carbonate/ethylene glycol containing 0.2% w/w NH_4F and 1.5% v/v H_2O; U_a=40 V; t_a=24 h and T=5 °C. *Insets* show lateral views for each case

The morphology of the nanostructures obtained was dependent on the amount of water in the electrolyte (Fig. 3b and c). By comparing both films, the effect of increasing potential was observed as an increase in the tube diameters and wall thickness. Figure 3c reflects the effect of a lower amount of water, showing a shorter nanotube layer, of approximately 40 μm of length. It has been previously reported that the tube length (for anodic oxide layers grown on different valve metals using non-aqueous electrolytes) is related to the electrolyte composition and not to the anodization time [37, 38]. The nanotube lengths are directly limited by the complete utilization of the active electrolyte species during the anodization time. Paulose et al. [38] observed this fact and found a relation for the optimum concentration of water for achieving the highest growth rates for different NH_4F concentrations. In this range of NH_4F and H_2O concentrations, the anodic dissolution due to the increased% w/w of NH_4F is compensated by the increase in the H_2O concentration and results in greater growth rates and correspondingly longer nanotubes lengths. The presence of a higher water content promotes the oxidation of the metal and enhances the chemical etching rate of the oxide structure in the presence of fluoride ions. Additionally, the presence of propylene carbonate seems to minimize the lateral dissolution inside the pore, which is evidenced as higher tube lengths using shorter anodization times (Fig. 3b), as compared with those obtained with low water content (Fig. 3c) or in the absence of propylene carbonate in the electrolyte [12, 13].

Figure 4 shows SEM images of titanium foils anodized for 6 h at constant voltage values of 40 V (Fig. 4a), 60 V (Fig. 4b) and 80 V (Fig. 4c) in a 50:50 propylene carbonate/ethylene glycol solution containing 0.2% w/w NH_4F and 3% v/v H_2O at 5 °C. A transition from an almost compact morphology to a tubular morphology of the oxide layers, by increasing the applied voltage, is clearly shown (Fig. 4a–c). In spite of the high voltage applied, the polarization time was not sufficient for the complete separation of the tubes and for the self-assembly of the nanotube layer (Fig. 4a), as is attained when the anodization time is increased (Fig. 3c)

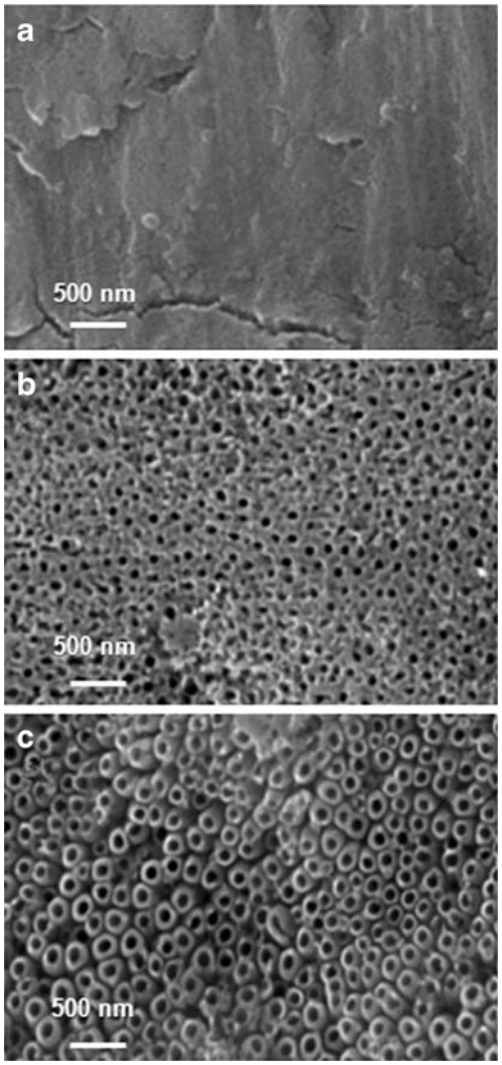

Fig. 4 Top view SEM images of the morphology of anodic TiO_2 layers grown in 50:50 propylene carbonate/ethylene glycol containing 0.2% w/w NH_4F and 3% v/v H_2O; t_a=6 h and T=5 °C for U_a=40 V (**a**), 60 V **b** and 80 V (**c**)

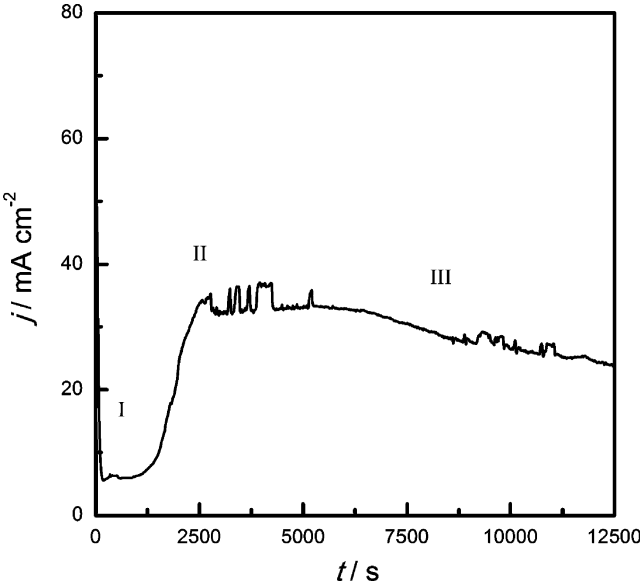

Fig. 5 Current density transient recorded at 5 °C for the anodization at 40 V of Ti in a 50:50 propylene carbonate/ethylene glycol containing 0.2 wt.% NH_4F and 1.5 vol.% H_2O solution

or when propylene carbonate based electrolytes are used. Notably, the low temperature employed limits the migration and the diffusion rate of the ions involved in the growth and etching of the oxide layer. These results are in line with the mechanistic aspects of the self-assembling process previously reported for nanotubes formed on other valve metals [1, 27, 37].

Figure 5 shows the initial part of the current density transient recorded at 5 °C for Ti anodization at 40 V for 24 h in a 50:50 ethylene glycol/propylene carbonate containing 0.2% w/w NH_4F and 3% v/v H_2O solution. The transient features are in line with the behavior usually found for the anodic oxidation of valve metals immersed in solutions containing fluoride ions and leading to self-organizing tubes [1, 27]. Initially, the current density quickly increases because of the active dissolution of Ti. Then, the titanium oxide layer that acts like a barrier begins to grow by a high field migration mechanism according to the following overall reaction:

$$Ti_{(s)} + 2H_2O_{(l)} \rightarrow TiO_{2(s)} + 4H^+_{(aq)} + 4\bar{e} \quad (1)$$

Meanwhile, the current decreases due to the film growth and the passivation of the surface (zone I). Simultaneously, a random dissolution process of the layer is promoted by the fluoride ions present in the electrolyte, which drives pit formation in the film, according to

$$TiO_{2(s)} + 6F^-_{(aq)} + 4H^+_{(aq)} \rightarrow TiF^{2-}_{6(aq)} + 2H_2O_{(l)} \quad (2)$$

Consequently, due to the pitting process, a porous structure nucleates, and the active area increases, while the current density rises to a maximum value (zone II). Afterwards, the current density is almost constant and shows a slight decrease (zone III). Because the system is under a constantly applied voltage, the electric field within the oxide is progressively reduced by the increase in oxide thickness and the process is limited by itself. During this time, the individual pores are separated, and self-assembled nanotubes are generated by continuous polarization in the presence of fluoride ions. The reason for the separation into tubes as opposed to the formation of a nanoporous structure is not yet entirely clear. However, it could be ascribed to the accumulation of fluoride species at the bottom of the tube, thus leading to the establishment of a weaker anion containing the TiO_2 structure between pores and neighboring tubes [1].

Electrochemical impedance spectroscopy analysis

To study the electrical and semiconducting properties of the anodic layers during the transition from a compact to a tubular morphology, electrochemical impedance spectroscopy measurements were performed with anodic TiO_2 layers grown at different potentials. Figure 6 shows Bode plots taken in the depletion zone at the open circuit potential (0.23 V) on nanotubular TiO_2 layers, obtained by anodizing Ti at different voltages for 6 h at 5 °C in a 50:50 propylene carbonate/ethylene glycol mixture containing 0.2% w/w NH_4F and 3% v/v H_2O. The morphology of these surfaces is shown in Fig. 4. At least two time constants are observed for the three conditions studied. This behavior could be attributed to the porous or nanotubular nature of the oxide layers. Similar behavior has been reported for anodic porous alumina films [47, 48] and nanotubular TiO_2 arrays [15, 49].

The results shown in Fig. 6 were interpreted by considering the "passive pit" model for porous films, as proposed by Jüttner [47]. Figure 7 shows a schematic representation of the Ti/TiO_2 layer/electrolyte interface

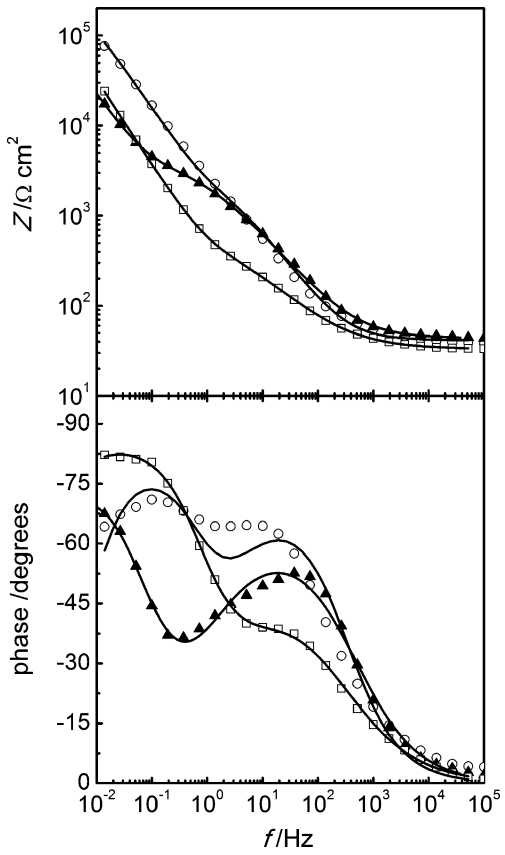

Fig. 6 Bode plots of anodic TiO_2 layers grown in 50:50 propylene carbonate/ethylene glycol containing 0.2% w/w NH_4F and 3% v/v H_2O; t_a=6 h and T=5 °C. U_a=40 V (*open circle*); 60 V (*filled triangle*) and 80 V (*empty square*). *Solid lines* represent best fits obtained using the equivalent electric circuit shown in Fig. 7c

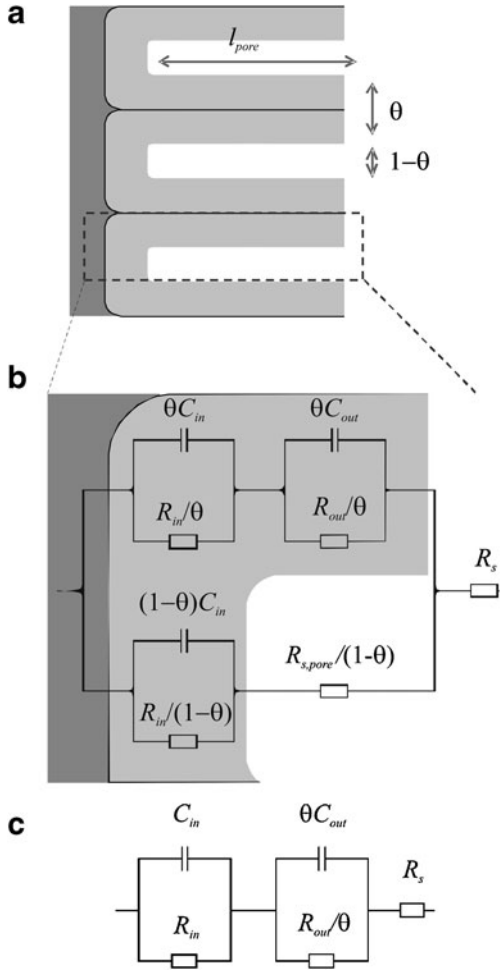

Fig. 7 **a** Scheme showing the Ti/nanotubular TiO_2/electrolyte interphase; **b** equivalent electric circuit for a porous film; **c** equivalent electric circuit simplified for $R_s > R_{s,\ pore}$

(Fig. 7a) and the corresponding equivalent electric circuit (Fig. 7b). The model considers a non-homogeneous film formed by a thin, barrier-type layer and a thick, porous layer on top. Each layer is a quasi-homogeneous oxide phase characterized by a parallel combination of capacitance C_i and resistance R_i (C_{in}, R_{in}, C_{out} and R_{out}). Constant phase elements, characterized by a frequency dispersion coefficient, n, instead of ideal capacitances, are used to take into account the frequency dispersion [50]. In addition, the solution resistance inside the film pores, $R_{s,\ pore}$, is considered only in the outer layer. The overall impedance is the sum of both contributions weighted by the coverage degree, θ. From the analysis of the circuit in Fig. 7b, it follows that $R_{s,\ pore}$ can be ignored when $R_{s,\ pore} < R_s$, thus simplifying the circuit to two parallel RC circuits connected in series, as shown in Fig. 7c. The drawback of this model is that the individual contributions of the porous film (the tube walls) and that of the underlying barrier oxide cannot be extracted from the experimental R_i and C_i values without knowledge of θ.

As a passive element, the $R_{s,\ pore}$ value is determined by the electric resistivity of the electrolyte, ρ_e, pore length, l_{pore}, and effective pore cross-section area, $(1 - \theta)\ A$, according to

$$R_{s,pore} = \rho_e \frac{l_{pore}}{(1-\theta)A} \quad (3)$$

Assuming a coverage of θ=0.9, a pore length of l_{pore} = 200 μm and an electrolyte conductivity of 12.89 mS cm^{-1} (corresponding to 0.1 M KCl at 25 °C), the solution resistance in the film pores is around 15 Ω cm^2. This value is slightly lower than the solution resistance values experimentally obtained, which were around 30–40 Ω cm^2 (see the Z value at high frequencies in Fig. 6). Using this approximation, the impedance spectra were fitted, and the best fittings obtained are shown as continuous lines in Fig. 6. The fittings are adequate to describe the full spectra, indicating that two different layers are present on average. The values obtained for the circuit elements (Table 1) indicate that there is a highly resistive inner layer ($R_{in} > > R_{out}$), whereas the outer layer is more conductive and defective ($n_{in} > n_{out}$). The capacitance values for the barrier layer increases with the applied potential, indicating that the inner layer thickness decreases, which can be interpreted as a transition from a mostly compact layer (Fig. 4a) to a porous layer, with increasing pore length or porosity with the applied potential (Fig. 4b and c). Other authors have interpreted the impedance spectra by considering the semiconducting properties of titania films formed by anodization in aqueous solutions containing hydrofluoric acid [15, 49].

Figure 8 shows Mott–Schottky plots for the samples shown in Figs. 4 and 6 at a frequency of 10 kHz in dark conditions. The Mott–Schottky analysis is valid in the depletion zone of the semiconductor and is based on the study of the variation of the differential capacitance of the space charge layer, C_{sc}, with the potential for a fixed layer thickness. It predicts a linear relationship of C_{sc}^{-2} with the applied potential, as described by the following equation for an n-type semiconductor:

$$\frac{1}{C_{SC}^2} = \frac{2}{\varepsilon_0 \varepsilon e N_D}\left[E - E_{FB} - \frac{kT}{e}\right] \quad (4)$$

where ε is the dielectric constant, ε_0 is the vacuum permittivity, e the electron charge, N_D is the donor density, E_{FB} is the flat band potential and k is the Boltzmann constant. Table 1 shows the numeric values of N_D and E_{FB}, which were calculated by considering a dielectric constant of ε=60 [51]. The positive slope indicates that the oxide films behave as an n-type semiconductor. According to Fig. 4, the series shows the transition from compact to nanotubular layers as discussed before, and the increase in the donor concentration reflects the growth of a defective outer layer. The dependence of the flat band potential with the anodized voltage indicates that this characteristic value can be modified by the morphological characteristics. In this case, the determination of the flat band potential according to the Mott–Schottky equation can be affected by a number of factors, e.g., high doping concentration (see Table 1), the presence of a high density of surface states attributed to the presence of TiO_2 nanotubes with a considerable number of grain limits, and the influence of diffusion-controlled processes that can be present inside nanotubes.

Photoelectrochemical measurements

Figure 9a shows the potentiodynamic j/E profiles obtained at 0.05 Vs^{-1} in 0.1 M KCl for a nanotubular TiO_2 layer (the morphology shown in Fig. 3c) and this layer sensitized by TCPP after 24 h of immersion (Fig. 9b), under darkness and illumination. In general terms, a notable increase in the oxidation current is observed when both oxide layer samples were illuminated. This photocurrent is associated with a series of processes occurring simultaneously in the semiconductor/electrolyte interface: photogeneration of $\bar{e}/h^+$ pairs, separation, recombination and charge transfer. It is well known that a higher photocurrent response corresponds to higher photoelectrochemical reactivity. However, it is possible to appreciate important differences between both interfaces. In dark conditions and in the negative scan, the TiO_2/electrolyte interface (Fig. 9a) shows a cathodic contribution that can be attributed to the hydrogen evolution reaction (HER). In the positive scan, an oxidation current can be observed at −0.70 V on the TiO_2/electrolyte interface. This feature could be due to the oxidation of the hydrogen intermediates previously formed in the negative scan, which inject electrons in the semiconductor. At potentials more positive than −0.25 V, the current decreases to the capacitive values. No oxidation

Table 1 Parameters obtained after fitting the experimental impedance results shown in Figs. 6 and 8

U_a (V)	R_s (Ω cm^2)	R_{in} (MΩ cm^2)	C_{in} (μF cm^{-2})	n_{in}	R_{out} (kΩ cm^2)	C_{out} (μF cm^{-2})	n_{out}	10^{+19} N_D (cm^{-3})	E_{fb} (V)
40	29.0	0.38	124	0.824	0.65	47.8	0.673	0.85	−0.09
60	43.4	0.36	530	0.885	3.03	94.7	0.692	1.30	−0.24
80	32.4	0.29	546	0.971	0.28	88.0	0.489	2.43	−0.44

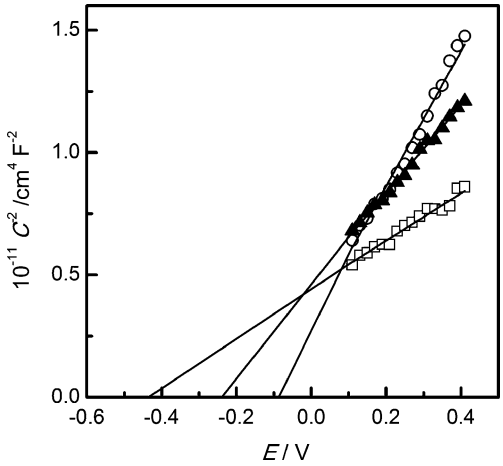

Fig. 8 Mott–Schottky plots of TiO_2 layers obtained in 50:50 propylene carbonate/ethylene glycol containing 0.2 wt.% NH_4F and 3 vol.% H_2O; t_a=6 h and T=5 °C. U_a=40 V (*open circle*); 60 V (*filled triangle*) and 80 V (*open square*)

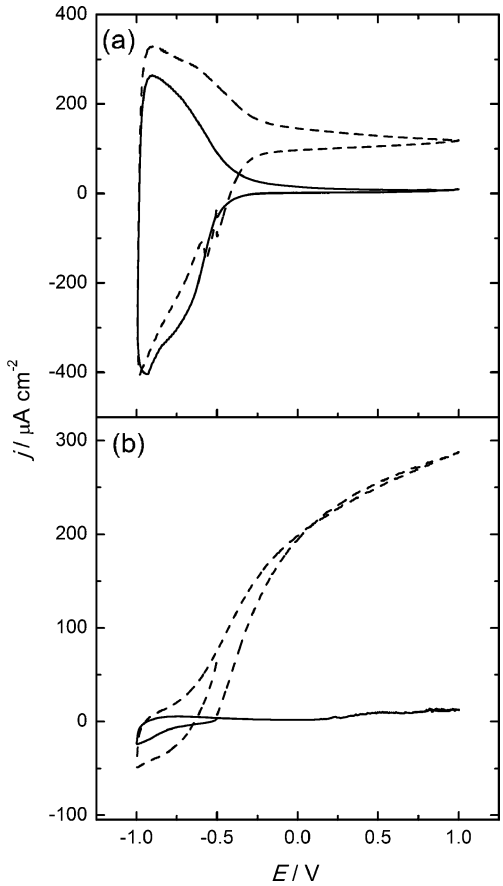

Fig. 9 Potentiodynamic j/E response at 0.05 V s^{-1} of TiO_2 layers in a 0.1 M KCl electrolyte. TiO_2 layers were obtained in 50:50 propylene carbonate/ethylene glycol containing 0.2 wt.% NH_4F and 1.5 vol.% H_2O; t_a=24 h and T=5 °C. U_a=40 V; in darkness (*solid line*) and under illumination (solar simulator) (*dashed line*) conditions; without dye **a** and after 24 h of immersion in TCPP solution (**b**)

current is observed because, in dark conditions, there is a negligible concentration of minority carriers (holes) in the valence band. On the TiO_2/TCPP/electrolyte interface (Fig. 9b) and in the negative scan, the HER process is weakly observable in this potential range. This behavior could be attributed to the increase in the overpotential for the HER due to the adsorbed TCPP film. No process is observed on TiO_2/TCPP/electrolyte interface in the positive scan. Under illumination and in the negative scan, no significant differences were observed in the TiO_2/electrolyte interface. However, an increase in current at −0.70 V in the positive scan can be observed. This fact can be attributed to the appearance of holes in the valence band, which are sent to the interface due to the depletion layer in the semiconductor at these potential values. At potential values more positive than −0.25 V, the photocurrent decreased. However, this time, it reached a limit value of −150 μA cm^{-2}, indicating the presence of a faradaic process attributed to water oxidation. The limit value could indicate the presence of a recombination process parallel to the Faradaic process, and, in this way, a steady state at this current value is produced independent of the band bending in the semiconductor. Considering the TiO_2/TCPP/electrolyte interface, no process is observed in the negative scan under illumination. In the positive scan at −0.70 V, a process occurs, and the current increases continuously at more positive potentials. This process is attributed to water oxidation, reaching higher photocurrent values than the TiO_2/electrolyte interface. This fact can be explained considering that the presence of the TCPP allows an increase in the photon absorptions of wavelengths in the visible range, generating TCPP* in an excited state, which injects electrons in the conduction band of TiO_2. This process increases the electrons leaving the semiconductor and contributing to the oxidation current. The holes photogenerated in TiO_2 can oxidize the water molecules in the electrolyte. Finally, increasing the electrons injected in the semiconductor increases the ratio of the Faradaic to the recombination current, indicating that the band bending allows a more effective charge carrier separation. The results obtained in terms of the water oxidation photocurrent were low compared to those obtained, for instance, by Mor et al. [27], using nanotube arrays in 1 M KOH solutions. These authors obtained photocurrents in the order of 15 mA cm^{-2}, while the photocurrents here were between 200 and 300 μA cm^{-2}. This difference can be principally attributed to the illumination intensity employed. These authors used 100 mW cm^{-2} 320–400 nm, whereas 4.0 mW cm^{-2} under solar simulation conditions were used here. With this illumination intensity, a minor quantity of photons with sufficient energy for electron/hole photogeneration will arrive on the electrode surface, and, thus, a minor water mass can be oxidized.

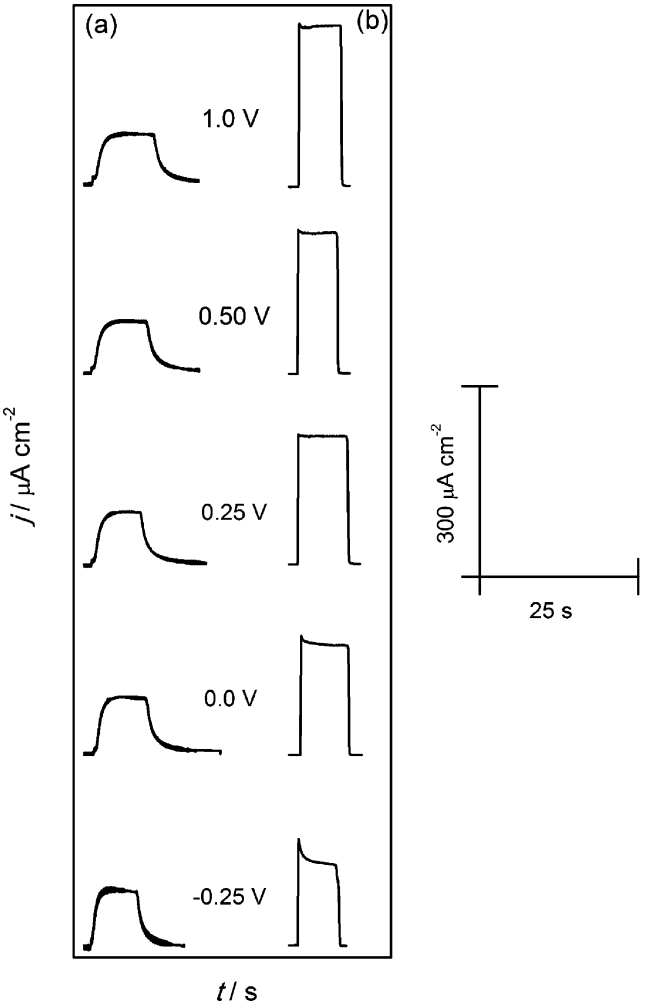

Fig. 10 Photocurrent transients at different potentials of TiO_2 layers grown in 50:50 propylene carbonate/ethylene glycol containing 0.2 wt.% NH_4F and 1.5 vol.% H_2O; t_a=24 h and T=5 °C. U_a= 40 V; without dye **a** and after 24 h of immersion in TCPP solution (**b**)

The photocurrent transients obtained for nanotubular TiO_2 layers with and without sensitization and by application of a square-amplitude light pulse of a constant light intensity and at potentials more positive than the flat band potential of the semiconductor electrode (−0.25–1.0 V) are shown in Fig. 10a without dye and Fig. 10b with TCPP. The processes involved correspond to the charging of the space charge zone of the semiconductor, which acts like a capacitor when the light is on. Then, the current observed, $I_{ph,\ in}$, corresponds to the charge carriers that were photogenerated accumulating in the space charge region. Later, the electron–hole pairs photogenerated are separated by the electric field applied in the space charge layer. According to the potential applied, electrons are sent toward the bulk of the material and holes toward the semiconductor/electrolyte interface. If a sufficient electric field is not present at the interface, electron–hole pairs are annihilated in a recombination process, decreasing the $I_{ph,\ in}$ to a steady-state current value, $I_{ph,\ st}$, corresponding to the sum of the recombination and faradaic processes. Therefore, the ratio $I_{ph,\ st}/I_{ph,\ in}$ indicates the fraction of Faradaic process occurring at the interface. If the photocurrent transient has a square form ($I_{ph,\ st}/I_{ph,\ in}$ = 1), it is an indication that more photogenerated charge is being used in a faradaic process. In contrast, a decrease in the photocurrent transient is an indication of a recombination process. For all potentials applied on the nanotubular TiO_2/electrolyte interface (Fig. 10a), the $I_{ph,\ in}$ increases approximately until 90 $\mu A cm^{-2}$, reaching a $I_{ph,\ st}$ of approximately the same value until the illumination is turned off. When the illumination is off, a transitory decay of the current is observed, indicating that the transfer of holes photogenerated previously continues for a few seconds. The negligible differences between the photocurrent values obtained at the different potential values is in agreement with the results obtained in the voltammetry study, indicating that an increase in the band bending does not improve the charge carriers separation. On the other hand, when sensitized nanotubular layers are employed (Fig. 10b), the photocurrent increases for all potentials tested. The results obtained in the conditions depicted in Fig. 10a and b are summarized in Table 2.

From the values observed in Table 2, it can be concluded that the system in the presence of dye presents the best

Table 2 Parameters obtained from the photocurrent transients observed in Fig. 10a and b

Interface	Potential (V)	$I_{ph,\ in}$ ($\mu A cm^{-2}$)	$I_{ph,st}$ ($\mu A cm^{-2}$)	$I_{ph,\ st}/I_{ph}$ ratio
TiO_2/electrolyte	−0.25	90	90	1.0
	0.0	96	96	1.0
	0.25	90	90	1.0
	0.5	91	91	1.0
	1.0	90	90	1.0
TiO_2/TCPP/electrolyte	−0.25	179	136	0.76
	0.0	200	185	0.93
	0.25	218	212	0.97
	0.5	243	237	0.98
	1.0	269	265	0.99

performance in terms of the photocurrent obtained for the water oxidation process. In fact, an increase in the potential applied on the interface improves the separation of the charge carriers because of the increase observed in the value of the $I_{ph,\ st}/I_{ph}$ ratio, up to approximately 1.0 at 1.0 V.

Conclusions

The results of the present work show that highly ordered and self-organized TiO_2 nanotubular layers can be grown by anodizing Ti in propylene carbonate and ethylene glycol electrolytes. The length of the nanotubes obtained depends on the water content in the electrolytic bath. The transition from an almost compact to a nanotubular morphology can be obtained by increasing the applied potential. Based on a porous model, it is possible to study the electric properties at different stages of the nanotubular layer growth by impedance measurements. The semiconductor behavior of the tubular oxides can be explained by considering the high-defect density in the nanotubes, which are in equilibrium with the underlying barrier layer. Photoelectrochemical measurements show that TCPP adsorbs onto TiO_2 nanotube arrays, facilitating the electron transfer from this dye to the conduction band of the semiconductor and, in this way, contributing to the oxidation current flowing in the external circuit. Given the low rate of recombination in its presence, it can be a potential photosensitizer for solar-energy conversion by TCPP-sensitized nanotubular TiO_2 electrodes.

Acknowledgements We thank the Dirección de Investigación e Innovación of the Pontificia Universidad Católica de Valparaíso (grant No. 037.108/2009 DII-PUCV) for financial support for this study. E. Muñoz and R. Henríquez thank Programa Bicentenario de Ciencia y Tecnología, PSD82. D. Oyarzún is grateful to the CONICYT for his thesis scholarship. M. López and O. Linarez thank the Consejo Nacional de Investigaciones Científicas y Técnicas of Argentina (CONICET), the Agencia Nacional de Promoción Científica y Tecnológica (ANPCYT), and the Secretaría de Ciencia y Tecnología (SECYT-UNC) for financial support. O. Linarez also thanks the CONICET for the fellowship grant.

References

1. Macak JM, Tsuchiya H, Ghicov A, Yasuda K, Hahn R, Bauer S, Schmuki P (2007) Curr Opin Solid State Mater Sci 11:3–18
2. Masuda H, Yada K, Osaka A (1998) Jpn J Appl Phys 37:L1340–L1342
3. Thompson GE (1997) Thin Solid Films 297:192–201
4. Chik H, Xu JM (2004) Mater Sci Eng R43:103–138
5. Zwilling V, Aucouturier M, Darque-Ceretti E (1999) Electrochim Acta 45:921–929
6. Gong D, Grimes CA, Varghese OK, Chen Z, Dickey EC (2001) J Mater Res 16:3331–3334
7. Macak JM, Tsuchiya H, Schmuki P (2005) Angew Chem Int Ed 44:2100–2102
8. Beranek R, Hildebrand H, Schmuki P (2003) Electrochem Solid-State Lett 6:B12–B14
9. Macak JM, Tsuchiya H, Taveira L, Aldabergerova S, Schmuki P (2005) Angew Chem Int Ed 44:7463–7465
10. Ghicov A, Tsuchiya H, Macak JM, Schmuki P (2005) Electrochem Commun 7:505–509
11. Ruan C, Paulose M, Varghese OK, Mor GK, Grimes CA (2005) J Phys Chem B 109:15754–15759
12. Paulose M, Shankar K, Yoriya S, Prakasam HE, Varghese OK, Mor GK, Latempa TA, Fitzgerald A, Grimes CA (2006) J Phys Chem B 10:16179–16184
13. Macak JM, Taveira LV, Tsuchiya H, Sirotna K, Schmuki P (2006) J Electroceram 16:29–34
14. Yin Y, Jin Z, Hou F, Wang X (2007) J Am Ceram Soc 90:2384–2389
15. Muñoz AG, Chen Q, Schmuki P (2007) J Solid State Electrochem 11:1077–1084
16. Paulosea M, Pengc L, Popatb KC, Varghesed OK, La Tempaa TJ, Baoa N, Desai TA, Grimes CA (2008) J Membr Sci 319:199–205
17. Schmuki P, Fujimoto S (2009) Electrochim Acta 54:5155–5162
18. Tsuchiya H, Macak JM, Sieber I, Taveira L, Schmuki P (2005) Small 1:722–725
19. Lee WJ, Smyrl WH (2008) Curr Appl Phys 8:818–821
20. Sieber I, Hildebrand H, Friedrich A, Schmuki P (2005) Electrochem Commun 7:97–100
21. Choi J, Lim JH, Lee SCH, Chang JH, Kim KJ, Cho MA (2006) Electrochim Acta 51:5502–5507
22. De Tacconi NR, Chenthamarakshan CR, Yogeeswaran G, Watcharenwong A, De Zoysa RS, Basit NA, Rajeshwar K (2006) J Phys Chem B 110:25347–25355
23. Hahn R, Macak JM, Schmuki P (2007) Electrochem Commun 9:947–952
24. Sieber I, Schmuki P (2005) J Electrochem Soc 152:C639–C644
25. Wei W, Macak JM, Schmuki P (2008) Electrochem Commun 10:428–432
26. Tsuchiya H, Schmuki P (2005) Electrochem Commun 7:49–52
27. Mor GK, Varghese OK, Paulose M, Shankar K, Grimes CA (2006) Sol Energy Mater Sol Cells 90:2011–2075
28. Chen X, Mao SS (2007) Chem Rev 107:2891–2959
29. Jiang G, Tang H, Zhu L, Zhang J, Lu B (2009) Sens Actuators B 138:607–612
30. Liu M, Zhao G, Zhao K, Tong X, Tang Y (2009) Electrochem Commun 11:1397–1400
31. Aravindan V, Vickraman P, Krishnaraj K (2009) Curr Appl Phys 9:1474–1479
32. Wei D, Zhou Y (2009) Ceram Int 35:2343–2350
33. Brunella MF, Diamanti MV, Pedeferri MP, Di Fonzo F, Casari CS, Bassi AL (2007) Thin Solid Films 515:6309–6313
34. Pulsipher D, Fisher ER (2009) Surf Coat Technol 203:2236–2242
35. Macak JM, Schmuki P (2006) Electrochim Acta 52:1258–1264
36. Bauer S, Kleber S, Schmuki P (2006) Electrochem Commun 8:1321–1325
37. Yasuda K, Macak JM, Berger S, Ghicov A, Schmuki P (2007) J Electrochem Soc 154:C472–C478
38. Paulose M, Prakasam HE, Varghese OK, Peng L, Popat KC, Mor GK, Desai TA, Grimes CA (2007) J Phys Chem C 111:14992–14997
39. Prakasam HE, Shankar K, Paulose M, Varghese OK, Grimes CA (2007) J Phys Chem C 111:7235–7241
40. Muraa F, Masci A, Pasquali M, Pozio A (2009) Electrochim Acta 54:3794–3798
41. Schmuki P, Tsuchiya H, Taveira L, Sirotna K, Macak JM (2006) Met Semicond 179–186

42. Wang C, Bahnemann DW, Dohrmann JK (2000) Chem Commun 16:1539–1540
43. Wang Y, Hao Y, Cheng H, Ma H, Xu B, Li W, Cai S (1999) J Mater Sci 34:2773–2799
44. Zhu K, Neale NR, Miedaner A, Frank AJ (2007) Nano Lett 7:69–74
45. Cherian S, Wamser CC (2000) J Phys Chem B 104:3624–3629
46. Grätzel M (2001) Nature 414:338–344
47. Jüttner K (1990) Electrochim Acta 35:1501–1508
48. Potucek RK, Rateick RG, Birss VI (2006) J Electrochem Soc 153: B304–B310
49. Muñoz AG (2007) Electrochim Acta 52:4167–4176
50. Macdonald JR, Barsoukov E (2005) Impedance spectroscopy: theory, experiment, and applications, 2nd edn. Wiley, New York
51. Taveira LV, Sagüés AA, Macak JM, Schmuki P (2008) J Electrochem Soc 155:C293–C302